Rapport BIPM-2006/01

Measurement of the Specific Heat Capacity of Graphite

S. Picard, D. T. Burns and P. Roger

International Bureau of Weights and Measures
Bureau International des Poids et Mesures
Pavillon de Breteuil
F-92312 Sèvres cedex France

January 2006

Measurement of the Specific Heat Capacity of Graphite

by S. Picard, D. T. Burns and P. Roger

Bureau International des Poids et Mesures, F-92312 Sèvres cedex France

Abstract

With the objective of implementing graphite calorimetry at the BIPM to measure absorbed dose, an experimental assembly has recently been constructed to measure the specific heat capacity of graphite. A status description of the apparatus and results from the first measurements are given. The outcome is discussed and the experimental uncertainty is reviewed.

1. Introduction

The long-term objective of absorbed dose calorimetry, recently initiated at the BIPM, is to develop a portable primary standard to measure absolute dose (or dose rate) of ionizing radiation in high energy, high dose-rate photon beams. Such measurements are exploited routinely where ionizing radiation is used for medical therapy.

Radiation impinging on a solid is either reflected, absorbed or transmitted depending on the frequency of the radiation and the character of the solid. The absorbed radiation, or some fraction of it, is transformed into heat through various physical processes. Hence, by exposing a solid to radiation, we can deduce the absorbed energy by measuring the associated temperature rise.

Many types of calorimeters have been designed, and calorimeters specially dedicated to the measurement of absorbed dose have been developed during the last 50 years. Reviews of the evolution can notably be found in [1-6].

The relevant physical properties of human tissue are similar to those of water. Recommendations have hence been given by international organizations to national metrology institutes (NMIs) to develop absorbed dose to water standards [7-10]. Several NMIs have developed water calorimeters. Among solid matter, graphite and some plastic compounds show a similarity to water with regards to ionizing radiation, and have been used to make calorimeters to measure absorbed dose. Graphite has been studied over the years and conversion factors for absorbed dose to water are known with acceptable uncertainty; the availability of Monte Carlo codes has improved this accuracy [11].

Many arguments for and against choosing a certain calorimeter material can be found. For the BIPM calorimeter, graphite was chosen due to:

- its similarity to water in terms of radiation interactions;
- its lack of thermal defects;
- its comparatively low specific heat capacity and good thermal conductivity;
- the possibility for compact technical solutions;
- the possibility to realize different designs of chambers to detect or avoid eventual systematic effects;
- the potential to provide information on W_{air}, the mean energy required to produce an ion pair in air.

Separating the equipment to measure the specific heat capacity from that to measure absorbed dose provides an opportunity to optimize each device in respect to geometry and surroundings. If the specific heat capacity of the absorber can be determined sufficiently accurately, the calorimeter can be simplified, made more robust and even demountable. For this reason, the measurements are divided into two parts:

1) To measure the specific heat capacity c_p of graphite, by measuring the temperature rise ΔT of a mass m associated with a well-known amount of injected electric energy E, i.e.

$$E = c_p \, \Delta T \;\; m, \tag{1}$$

or

$$c_p = \frac{E}{\Delta T \cdot m}. \tag{2}$$

2) To measure absorbed dose D_g, or dose rate, of ionizing radiation to graphite, where a graphite calorimeter is exposed to a high-energy photon beam, exploiting the fact that

$$D_g = E \,/m = \; c_p \, \Delta T. \tag{3}$$

This report concentrates on the first part, i.e. the measurement of the specific heat capacity of graphite using equation (2). The principle of the measurements is first described, followed by a description of the experimental apparatus. Preliminary results are discussed, and the experimental uncertainty is reviewed.

2. Experimental realization

The measurement apparatus constructed by the absorbed dose calorimetry group at the National Physical Laboratory (UK) has been a source of inspiration during the development of the BIPM specific heat measurement [12]. The basic technique consists of heating a well-known quantity of graphite using an accurately determined amount of energy, and measuring the temperature rise.

A schematic representation of a graphite cylinder equipped with three thermistors is shown in figure 1-a. One thermistor acts as the heating element. Two sensing thermistors are introduced, connected to a d.c. Wheatstone bridge (figure 1-b), whose output signal is a function of temperature. The power through the heating thermistor can be measured as a function of time, where the integral in time of the total power corresponds to the energy injected (figure 2-a). An ideal simultaneous bridge signal as a function of time is shown in figure 2-b, where the temperature rise is indicated. If the mass has been correctly determined, these parameters are sufficient to calculate the specific heat capacity.

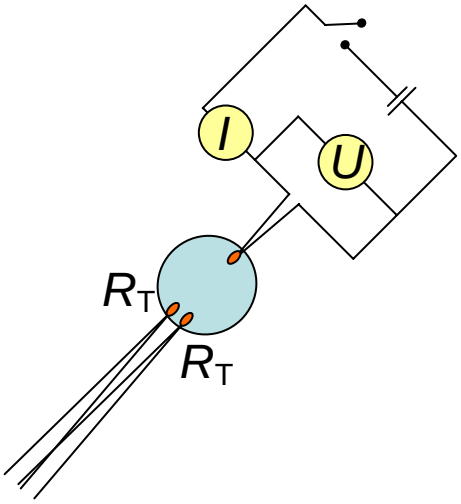

Figure 1-a. Schematic diagram of a graphite sample equipped with three thermistors. One thermistor heats the graphite. The other two, connected to a d.c. Wheatstone bridge, serve to measure temperature.

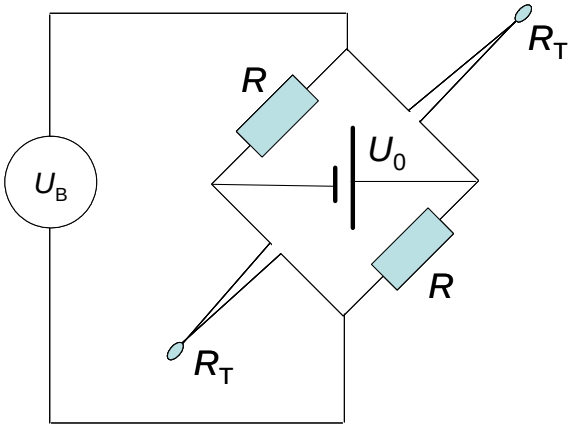

Figure 1-b. Wheatstone bridge containing two thermistors of the same resistance value, R_T, in opposite arms. The bridge is supplied by an in-house stable d.c. power supply at $U_0 = 1.14$ V, and the output signal U_B is measured using a commercial nV-meter.

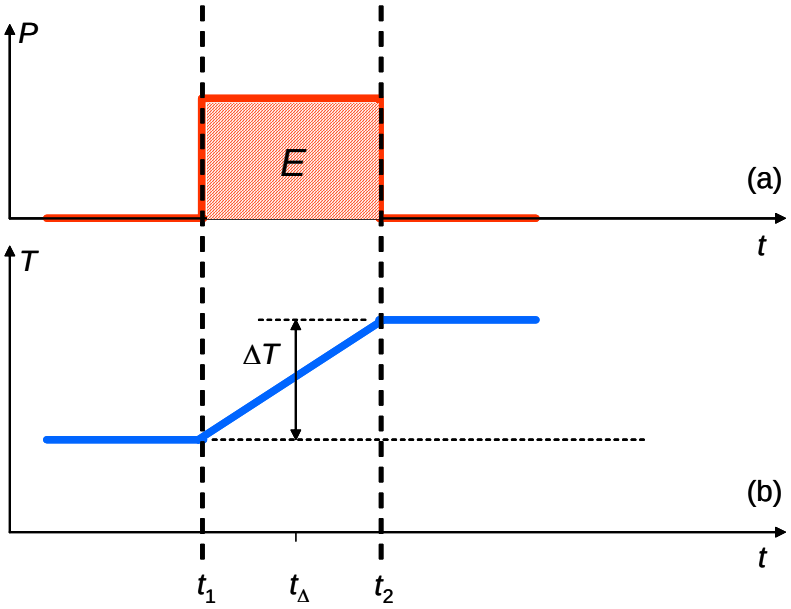

Figure 2-a. Power P through the heating thermistor depicted as a function of time t, where the total energy E is represented by the dashed area. **b)** Ideal instantaneous and simultaneous bridge signal, where the temperature T is shown as a function of time. The sample is heated between $t = t_1$ and $t = t_2$.The corresponding temperature rise is indicated as ΔT and is located at time t_Δ. In this ideal case, ΔT is not dependent upon t_Δ.

Three important issues need to be taken into account:

a) Specific heat capacity is temperature dependent. It is therefore necessary to measure the specific heat capacity over the entire temperature range to be used for the calorimeter.

b) Temperature exchanges will alter the results and might introduce statistical and systematic uncertainties in the interpretation of the temperature rise.

c) Any material in contact with graphite having a different specific heat capacity than graphite, such as the thermistor beads, are regarded as impurities, and introduce a systematic uncertainty unless their mass and specific heat capacities are taken into account.

To determine the specific heat capacity requires a measurement of the mass, injected energy and temperature rise of the sample. All these measurements were carried out in an air conditioned laboratory. The measurement sequences are computer controlled, and the analysis of experimental data is to a large extent automated. Each step in the realization of these measurements is described below.

2.1. Determination of mass

The preparation of the graphite samples requires care concerning size, relative position in the raw material, mass, impurities, and bulk density.

2.1.1. Size

A series of samples in the form of cylinders was machined from the same ultra-pure graphite block manufactured by Carbone Lorraine. The term ultra-pure indicates that the ash content is less than 5 parts in 10^6. In total, 11 cylinders of three different dimensions were machined. The dimensions of the cylinders was chosen so the mass is, at least, 10^4 larger than the mass of a thermistor. The cylinders have the same surface area, but different surface-to-volume ratios (*S*/*V* ratio). Their relative positions in the graphite block are indicated in figure 3. The nominal dimensions and *S*/*V* ratios are listed in table 1. One of the cylinders of series $\mathcal{A}$ will be the core of the planned calorimeter; these have the largest *S*/*V* ratio (this non-ideal shape is necessary for radiological reasons). The cylinders $\mathcal{B}$ have the smallest *S*/*V* ratio, where the height is equal the diameter. The cylinders C have a *S*/*V* ratio between those of $\mathcal{A}$ and $\mathcal{B}$.

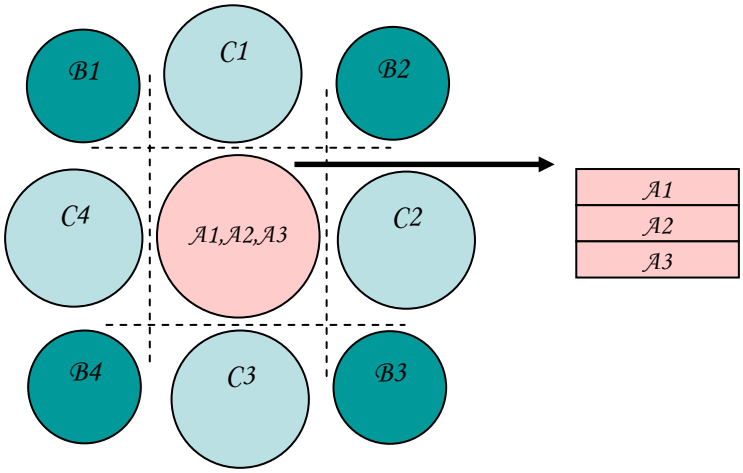

Figure 3. Relative positions and dimensions of the graphite samples before machining from the graphite block. They all have the same surface area, but different *S*/*V* ratios. The nominal dimensions and *S*/*V* ratios are listed in table 1.

Table 1. Nominal height (h), diameter (Φ), volume (V) and surface area (S) of the machined graphite cylinders. The parameter n indicates the number of samples.

cylinder	n	h / mm	Φ / mm	V / mm^3	S / mm^2	S/V ratio / mm^{-1}
$\mathcal{A}$	3	10.0	45.0	15.90×10^3	4.59×10^2	0.029
$\mathcal{B}$	4	31.2	31.2	23.85×10^3	4.59×10^2	0.019
C	4	19.5	38.0	22.11×10^3	4.60×10^2	0.021

To allow a precise determination of their volume, the cylinders have no bevelled edges. They are machined using no grease and, when handled, the operator wears gloves. The surfaces are polished.

2.1.2. Weighing

The mass of the graphite samples was measured using a Mettler H15 balance. This balance allows mass measurements up to 160 g, with a resolution of 0.1 mg. The balance is located in the ionizing radiation (RI) building in an air-conditioned laboratory where ambient temperature, atmospheric pressure and humidity are stabilized and monitored. The balance is calibrated by the Mass section at the BIPM.

To control the quality of the long-term stability of the measurements, a reference mass of similar weight in Dural® was fabricated. The reference mass was first measured using a calibrated high precision balance in the Mass section. This reference mass was then re-measured for each measurement series made.

When measuring each graphite sample, the sample was first put into a temperature controlled oven at 110 °C, according to the recommendations given in [13-15]. While cooling, it was placed in a recipient filled with a desiccant until ambient temperature is reached. It was then placed onto the balance using soft-tipped forceps. The weighings were repeated for each sample, controlling the zero reference between measurements.

The mass of each sample was determined through the mean value of these determinations, corrected for the air buoyancy effect according to [16,17], where the temperature, relative humidity and atmospheric pressure were taken into account. The mass was determined using the RI balance with a relative uncertainty of 2 parts in 10^5.

2.1.3. Density

Knowledge of the density is needed for the air buoyancy correction and for any future use of a sample in the calorimeter. It is also of interest to compare the density of the sample with the measured specific heat capacity. The bulk density of each sample was therefore determined. The mass measurement is described in section 2.1.2. The dimensional measurement was made using a 3D-measuring machine, offering a resolution of 1 µm and an estimated relative uncertainty of 1 part in 10^3. The densities in kg/m^3 are listed in table 2. The density of the cylinders $\mathcal{A}$ will be determined to higher accuracy later, being crucial for the future calorimeter. No obvious tendency in bulk density as a function of the relative position of the sample can be resolved. The unweighted mean of the bulk density ρ is

$$\rho = 1780 \text{ kg/m}^3 , \quad u_c = 2 \text{ kg/m}^3 ,$$

where u_c is the standard uncertainty of the distribution.

Table 2. Measured bulk density in kg/m^3 for each sample, where the place in the table corresponds to its relative position (figure 3). The statistical uncertainty in the last digit is indicated within parenthesis.

B1 1780.5(5)	*C1* 1780.9(7)	*B2* 1778(2)
C4 1778.9(7)	*A1* 1781(2) *A2* 1779(2) *A3* 1777(2)	*C2* 1780.2(7)
B4 1778(2)	*C3* 1779.4(7)	*B3* 1778.7(7)

2.2. Determination of electrical energy

The thermal energy injected into the graphite comes from the electric current supplied to the thermistor being transformed into heat. Power is the time derivative of energy. Therefore, an electric circuit was made to measure the power developed in the thermistor as a function of time. Several numerical methods exist to reduce uncertainties due to integration. The simplest way is to use a short integration step compared to the integration interval. This was achieved by using a commercial data acquisition (DAQ) card connected to a computer, allowing the high-speed collection of a large number of measurements. A typical acquisition-rate of 500 samples per second was chosen, resulting in a collection of nearly 150000 data during one scan.

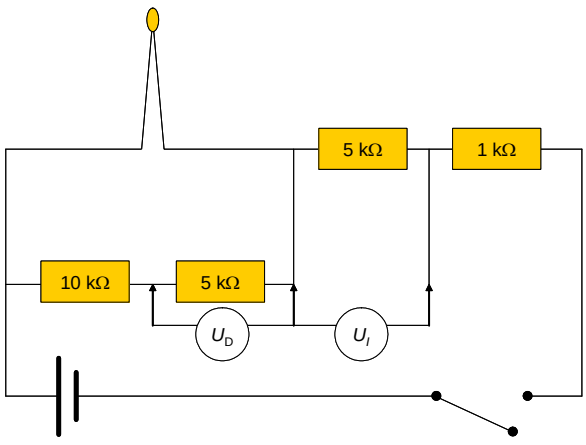

Figure 4. Voltage dividing electric circuit consisting of resistors with tight tolerance and low temperature coefficient. The signals U_D and U_I were recorded via a data acquisition card.

The electric circuit (figure 4) was adapted to obtain a reasonable temperature rise while respecting the power limits of the thermistor, and also to set the detection amplitude to obtain the best signal-to-noise ratio (S/N) provided by the acquisition card. The resistors used were of low temperature coefficient, tight tolerance and were initially measured using a calibrated resistance-meter. A d.c. voltage supply of 24 V generates the electric energy, commuted by a relay. Two voltage signals were recorded: U_D linked to the voltage applied over the thermistor and U_I representing the thermistor current. The energy is calculated knowing U_D, U_I and the resistor values. An example of the measured U_D signal is shown in figure 5. The small asymmetry at the beginning of the temperature rise, enlarged in the figure, is due to the rapid decrease of resistance when the thermistor is first heated.

The applied integration method results in a relative uncertainty of 2 parts in 10^5. The relative difference in calculating energy if the integration is made for the whole scan, including the zero signal, or only while heating is 6 parts in 10^7.

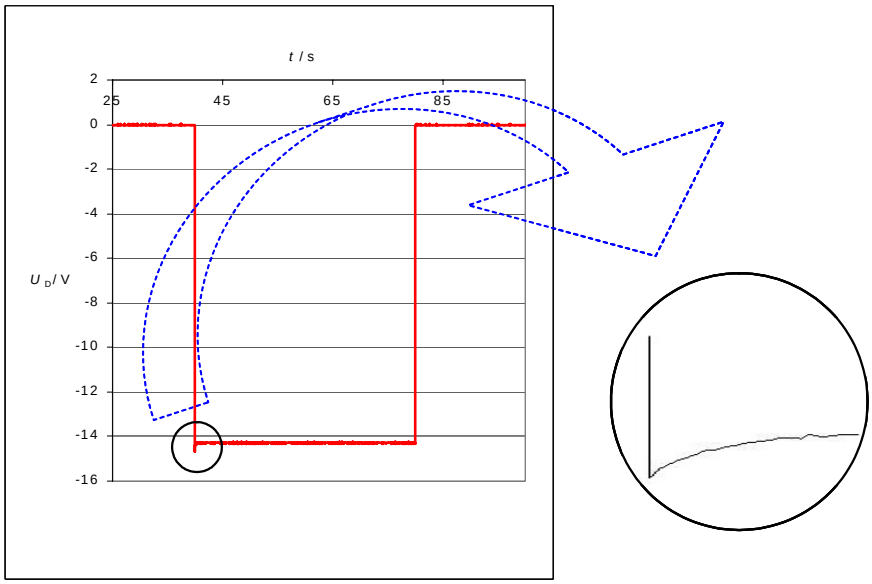

Figure 5. Voltage signals U_D depicted as a function of time t. The asymmetry observed in the beginning of the temperature rise, enlarged in the figure, is due to the decrease of resistance when the thermistor is heating.

2.3. Determination of temperature rise

2.3.1. A two-thermistor Wheatstone bridge and its temperature calibration

To measure the temperature rise, a configuration using two thermistors in opposite arms was chosen, *c.f.* figure 1-b. The resulting signal U_B is

$$U_B = U_0\left(\frac{R_T}{R_T + R} - \frac{R}{R_T + R}\right), \tag{4}$$

where U_0, R and R_T represent the voltage supply amplitude, a fixed resistance and the thermistor resistance, respectively. This configuration generates a signal that is twice as large than if one single thermistor was used.

Two glass beaded negative-temperature-coefficient thermistors, 1.8 mm long with a bead diameter of 0.38 mm, were glued with an epoxy resin having a good thermal conductivity into holes of slightly larger dimensions in the graphite. The thermistors were placed at the half-height of the cylinder and are equipped with long (2 m) insulated leads.

The graphite cylinder and the Wheatstone bridge assembly were calibrated against a temperature-calibrated platinum resistance thermometer (PRT). The graphite cylinder is placed in thermal contact within a copper recipient, into which the calibrated PRT can be introduced, as shown in figure 6. The detector thermistor wires are connected to an internal connector linked to the bridge and connected to a nano-Volt meter. The copper cylinder is sealed and immersed in a water-bath with a temperature stability of a few mK.

The recent purchase of a new temperature stabilized water tank provides an element for a reliable calibration which is not limited by environmental changes. Access to a PRT bridge which can be piloted from a computer allows automatic calibration of each test sample, while the temperature of the bath is varied in steps of about 0.5 °C from 19 °C to 28 °C.

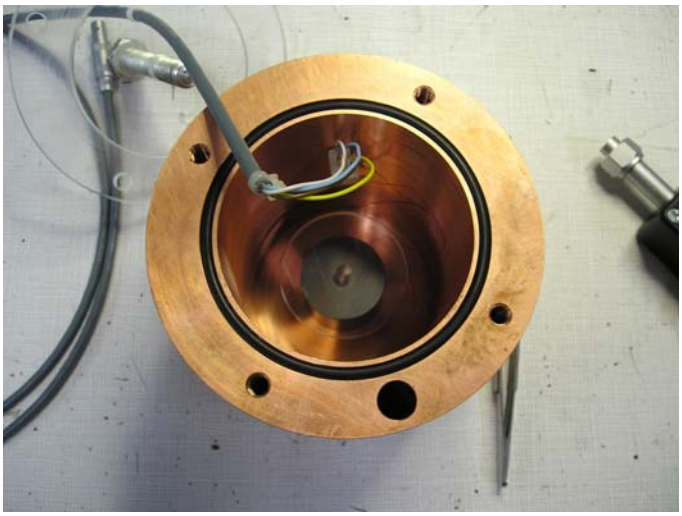

Figure 6. Copper recipient designed to contain the samples to be temperature calibrated and a PRT. The container is sealed before being immersed in water with a temperature stability of a few mK.

A fit of the experimental data, where the PRT temperature is plotted as a function of the bridge signal U_B, using a second order linear polynomial, gives

$$T(U_B) = [(a_0 + T_0) + a_1 \cdot U_B + a_2 \cdot U_B{}^2] \text{ K}, \tag{5}$$

where U_B is expressed in V, and where $T_0 = 273.15$ K. Since it is the temperature changes that are of primary interest, the derivative Θ is calculated according to

$$\Theta = \frac{dT}{dU_B} = [a_1 + 2 \times a_2 U_B] \text{ K/V}. \tag{6}$$

The combined standard uncertainty of the derivative, $u_c(\Theta)$, can be expressed as

$$u_c(\Theta) = \sqrt{u^2(a_1) + 4U_B{}^2 u^2(a_2) + 4U_B r_{12} u(a_1) u(a_2)} \text{ K/V}, \tag{7}$$

where $u(a_1)$ and $u(a_2)$ are the standard uncertainties of a_1 and a_2, respectively, and r_{12} is the correlation factor [18].

Sample data for a temperature calibration are shown in figures 7-a to 7-c. The derivative for this example is

$$\Theta = -45.16(1) + 5.6(2) U_B \text{ K/V}, \tag{8}$$

where the standard uncertainty of the parameters are indicated within parentheses. The minimum relative standard uncertainty for this measurement range is calculated to be 2.1 parts in 10^4.

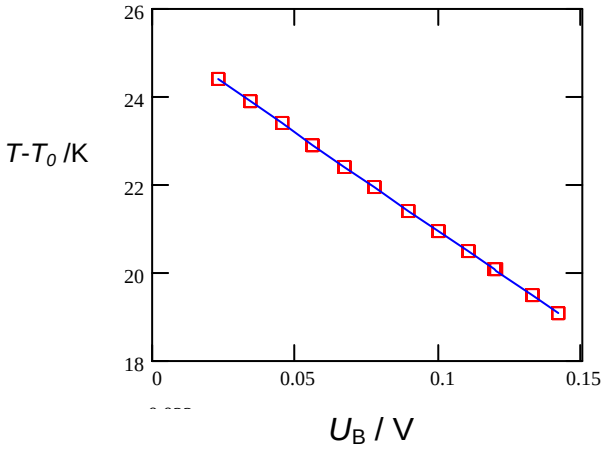

Figure 7-a. Measured temperature (T-T_0), plotted as a function of the bridge signal U_B.

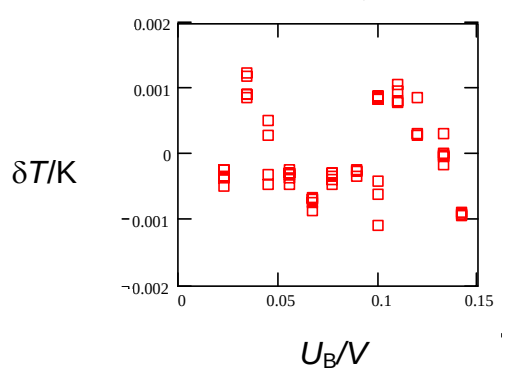

Figure 7-b. Difference δT between the observed temperature T_{obs} and the calculated temperature T_{calc}, using the fitted parameters from (5).

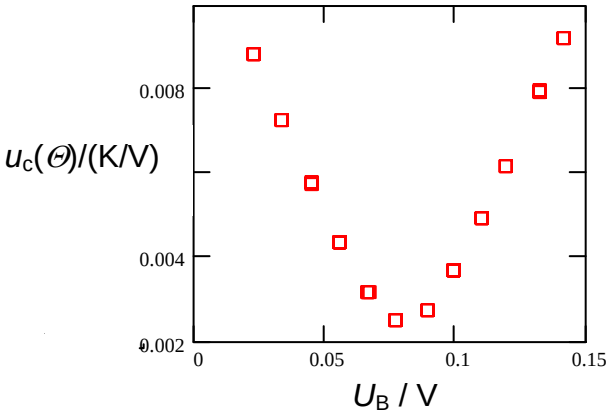

Figure 7-c. Combined standard uncertainty of the derivative Θ plotted as a function of the bridge signal U_B.

2.3.2. Realization of a stable d.c. voltage for the Wheatstone bridge

A stable d.c. voltage supply was needed for the Wheatstone bridge. The essential charactersistics of the supply are:

- a short term noise allowing a resolution of 10 µK, and
- a long-term stability superior to 1 part in 10^3 between recalibrations.

A design, similar to that of the NPL electron-beam calorimeter [19], was made.

A resolution of 10µK demands a resolution in voltage of some parts in 10^7. For this reason, care was taken to reduce the short-term noise resulting from cabling, grounding, shielding and filtering. However, the influence of the power supply noise on the bridge measurements is damped by the null-detector characteristic of the bridge, where the noise will become more important the further out-of-equilibrium the bridge is operated. Care was taken to choose electrical components of low thermal sensitivity, including a high-performance voltage reference. The power supply is also working in a temperature controlled area. The electrical scheme is shown in figure 8. The amplitude was chosen around 1 V, to reduce self-heating of the thermistors. Applying 1.14 V, the total self-heating in the graphite sample is estimated to be less than 30 µW.

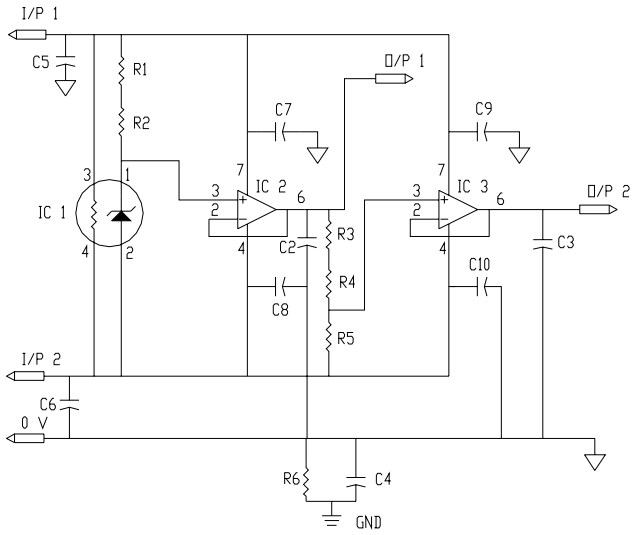

Figure 8. Electric scheme of the d.c. voltage bridge power supply. The resistances R_1, R_3, R_4 = 2.5 kΩ, R_2 = 5 kΩ, R_5 = 1 kΩ, R_6 = 100 Ω. The capacitors $C_2 - C_{10}$ = 10 nF. IC_1 represents a stable voltage reference LM399, and IC_2 and IC_3 symbolize operational amplifier OP27.

The short-term stability is illustrated by the relative Allan standard deviation (sometimes also called two-sample standard deviation) [20] in figure 9, where the short-circuited commercial nV-meter is represented by open squares. The use of a short-circuited cable connected to the meter gives a relative voltage stability indicated by black squares. When the power supply is loaded by a 10 kΩ resistance, the stability decreases. It reaches a minimum of 3 parts in 10^7 at 0.8 s, and more than 1 part in 10^6 at some tens of seconds (black triangles). The relative Allan standard deviation for a Wheatstone bridge at 10 kΩ is shown for comparison, illustrating the cancellation of short-term noise from the supply by the bridge (diamonds). Maximum stability is reached at about 15 s, which suggests that even some drift is cancelled by the bridge configuration. A pre- and post-heating time of about 40 s was chosen as a compromise to have a reasonable number of data to fit with a stability of a few parts in 10^8. For comparison, the $\tau^{-1/2}$ slope (Johnson noise) and the τ slope for thermal linear drift are also indicated in the figure.

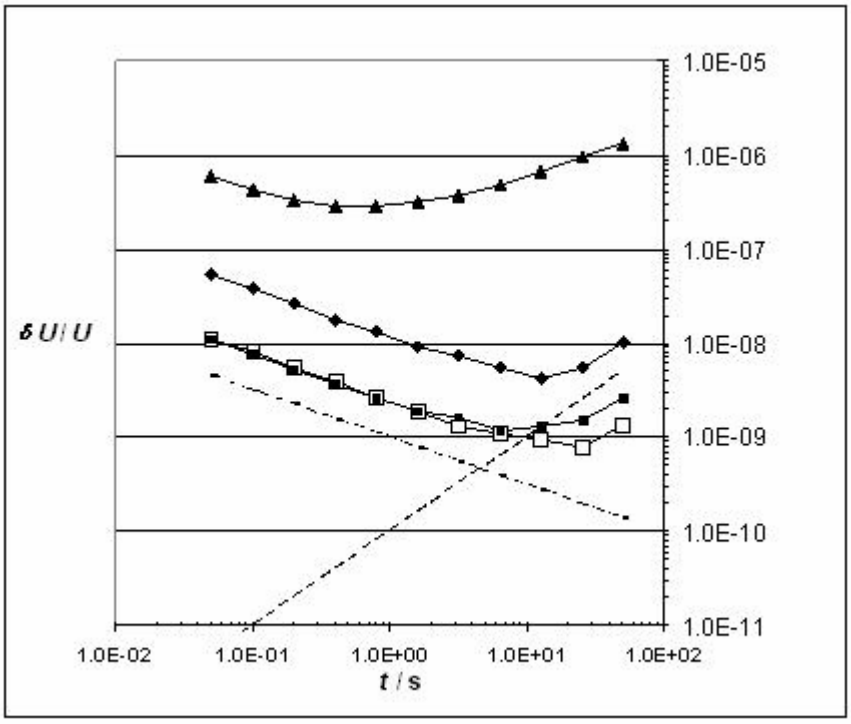

Figure 9. Short-term stability illustrated in terms of the relative Allan standard deviation. Open and black squares represent the short-circuited nV-meter without and with the connecting cable, respectively. Diamonds represents a Wheatstone bridge signal at 10 kΩ powered by the d.c. power supply, while the triangles shows the stability of the power supply loaded by a 10 kΩ resistance. The latter two curves show the partial cancellation of short term power supply noise by the bridge. For comparison, the $\tau^{-1/2}$ slope and the τ slope are also indicated in the figure.

2.3.3. Heat loss

Three mechanisms for heat loss are possible: conduction, convection and radiative heat transfer. Any loss will introduce an uncertainty in the measurement results by introducing a time-dependence that can be ambiguous to interpret due to the comparatively large time constants for temperature. Several methods can be envisaged to reduce heat loss.

2.3.3.1. Convection

Heat can be transported by convection phenomena, arising from the turbulence in a gas due to temperature differences in space. Convection can be avoided if a sufficiently high vacuum is applied to the contained volume. A stainless steel container, equipped with vacuum flanges and signal transmission connectors, was fabricated. The container can be temperature controlled by several heating elements attached to the external surface, connected to a commercial low-cost temperature regulator. The container was mounted in a Styrofoam® box, and a pump system was connected to evacuate the container, whereby the pressure could be controlled. A pressure of some mPa allow to neglect heat loss arising from convection [21]. When installing the graphite cylinder into the vacuum chamber, the electric wires were soldered onto the signal transmission

connectors and the cylinder itself was placed on a three-leg support, located in the bottom of the container.

2.3.3.2. Conduction

The vacuum chamber not only eliminates convection effects – it also reduces heat conduction through air (figure 10). Compared to the ideal curve traced in figure 2-b, the solid curve shows the total heat loss at atmospheric pressure and the dotted curve shows the heat loss when the vacuum has been attained. The losses are here reduced by a factor of 5, from 3.6 mK/min to 730 µK/min.

Unfortunately, other paths for conduction are still present: heat can be transported via the cylinder support and through the six wires connected to the thermistors. Different materials of the three-leg support were tested, such as stainless-steel needles, Styrofoam and wood. A satisfactory result was obtained using sharpened wooden tooth-picks. Another method, employed at the NPL [12] is to suspend the cylinder using two of the thermistor wires. This realization was tested, but no reduction of heat loss was observed, and the simpler choice of a mechanical support was maintained.

Heat transport via the wires is expected to be greater for the heating thermistor than for the two bridge thermistors. When measuring the resistance of the heating thermistor while heated, the temperature of the thermistor bead was registered above 100 °C. This local heat source dissipates its energy over the graphite cylinder, inducing a global temperature rise of some tens of mK of the mass. However, due to the large temperature gradient between the thermistor bead and the external connections, local heat will be lost via the wires. Furthermore, this potential heat loss will only be present during the heating period. The loss through the bridge wires will be of less importance, as their temperature gradients are much smaller. The heating wire was therefore wound tightly around the graphite cylinder to allow a re-absorption of the lost heat. However, these wires will influence the measured specific heat capacity – an effect that is discussed in section 3.2.

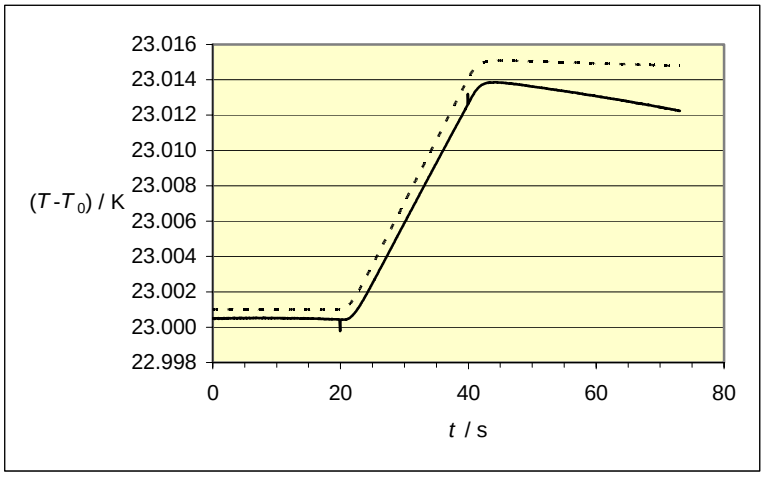

Figure 10. Illustration of reduction of heat loss by applying a vacuum. The solid curve, where no vacuum is present, shows a larger difference in pre- and post-heating slopes for the same amplitude of signal as the dotted curve, when a vacuum of some 10^{-4} Pa has been achieved. The two spikes are provoked by the power switch mechanism and demonstrate the time offset between electrical heating and detection of a temperature rise.

This heat loss is greater for larger wire diameter and should decrease if the wires are longer. A small reduction of heat loss was observed in changing the diameter of the connecting wires from 80 µm to 50µm. A system where a considerable length of wire was wound around hollow cylindrical plastic holders of small mass was also tested but no significant improvement was observed, perhaps due to a heat-sink effect from the plastic cylinders.

2.3.3.3. Radiative heat transfer

The remaining source of heat loss is radiative heat transfer. Factors such as surface quality and reflection coefficients will influence the exchange of radiation between two bodies if they are at different temperatures. Graphite has a large emissivity coefficient, i.e. it is susceptible to radiate heat. However, if the radiation is reflected back to the source, the source can be considered to be isolated in this respect. Initially, a mirror system of six flat gold mirrors was mounted around the graphite cylinder to recover radiative heat; the reflective coefficient of gold is larger than 99 % at 10 µm, the wavelength region for thermal radiation. The heat loss was thus reduced by about 25 %. Replacing the flat mirrors by two hemi-spherical dewars whose concave surfaces were gold-coated reduced the heat loss by 30 %.

An attempt to estimate the radiative heat loss after inserting the gold-coated dewars can be made, using a simplified expression for radiative heat transfer Q_{rh} for specular reflections [22], where

$$Q_{rh} = \frac{A_1 \sigma \cdot \left(T_1^4 - T_2^4\right)}{1/\varepsilon_1 + 1/\varepsilon_2 - 1}. \qquad (9)$$

Here σ represents the Stefan-Boltzmann constant. Assuming the emissivity coefficient $\varepsilon_1 = 0.9$ for the graphite cylinder of area A_1, and $\varepsilon_2 = 0.1$ for the gold-coating, with a corresponding temperature difference of $T_1 - T_2 = 10$ mK, the radiative heat transfer is estimated to be $Q_{\mathrm{rh}} \approx 16$ µW. For a graphite cylinder with minimum S/V ratio and mass 50 g, this corresponds to a loss of 0.5 µK/s. However, a loss of 2 µK/s was observed. With the argument that the gold surface is not of optical quality and that some of the radiated heat will not be fed back to the graphite due to the geometry, one can only roughly estimate the proportion of the remaining heat loss that originates from radiation and conduction.

2.3.4. Summary of reduction of heat loss

An illustration of these improvements is given in figure 11. Here the slope of each curve represents the increasing loss through a series of measurements. Adding two turns of heating thermistor wire around the graphite cylinder, as described in section 2.3.3.2. clearly reduces the heat loss. The arrangement of flat gold mirrors surrounding the graphite sample, further reduces the loss. Most of the wires, of a diameter of 80 µm, were replaced by 50 µm wide copper wires, giving a slight improvement. The use of two half spherical gold plated dewars results in a further reduction of heat loss.

Despite the efforts on heat loss reduction, a possible correlation between the temperature variations in the laboratory and the data was observed. An illustration of the influence of the laboratory temperature variations combined with temperature variations of the vacuum chamber is shown in figure 12-a. The successive measured heat capacity c_p shows a spread which is unlikely to be statistical. The measured laboratory temperature in

arbitrary units is shown in figure 12-b. A factor will be included into the measured ΔT, due to radiation heat transfer in combination with a laboratory temperature drift.

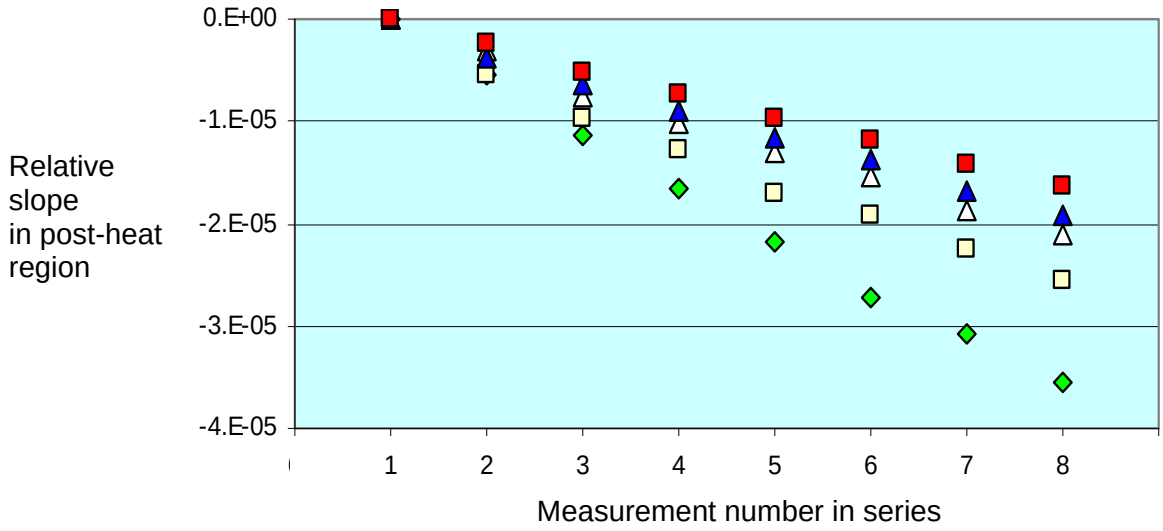

Figure 11. The relative change in post-heat loss given in arbitrary units for four series of measurements. The largest loss (green diamonds) represents a sample in vacuum having 4 turns of wire from the heating thermistor wound around the graphite cylinder. The losses were successively reduced by i) adding 2 turns of wire – light yellow squares, ii) surrounding the sample by flat gold mirrors – white triangles, iii) reducing the wire diameter from 80 µm to 50 µm – dark blue triangles, iv) replacing the flat mirror system by two semi-spherical gold plated dewars – red squares.

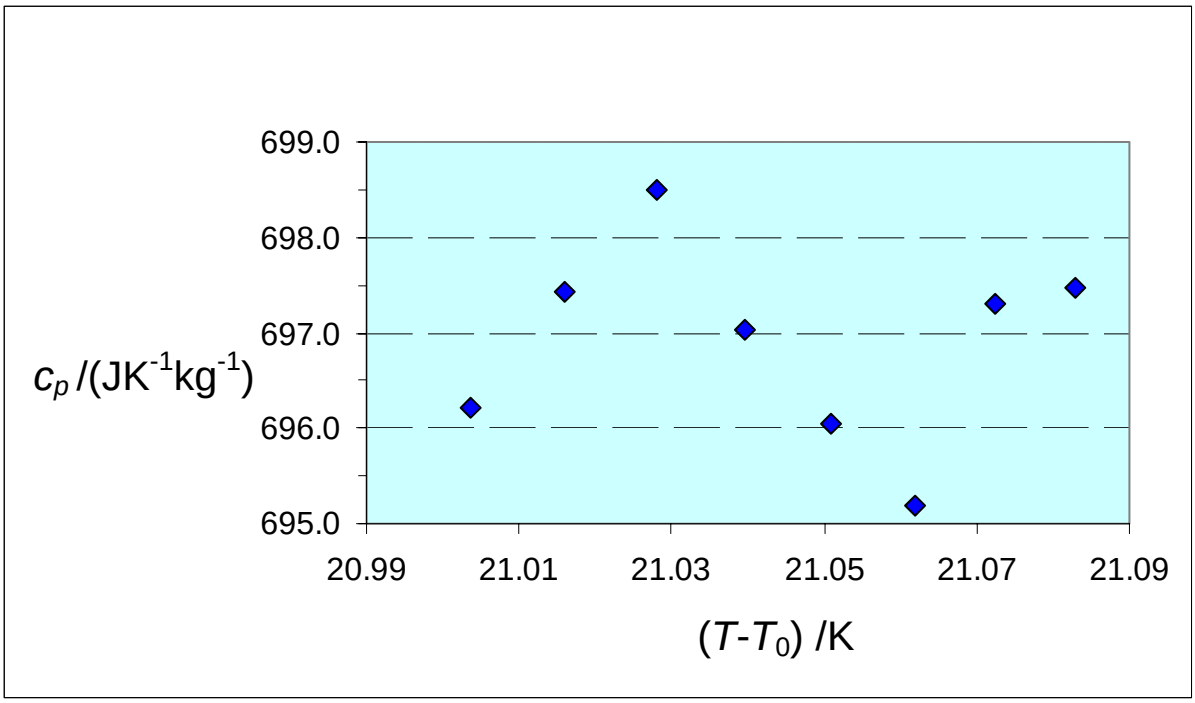

Figure 12-a. The laboratory temperature variations combined with temperature variations of the vacuum chamber can add a systematic shift of c_p.

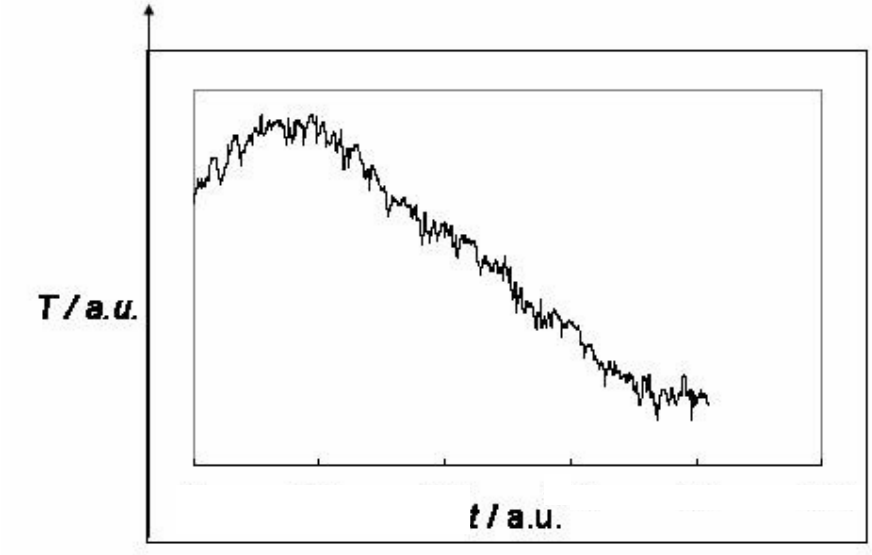

Figure 12-b. Plot of the temperature variations in the laboratory. The amplitude represents a temperature difference of 1.5 K in the laboratory.

2.4 Experimental equipment

Several samples were measured while the experimental set-up still was evolving. To reduce the effects of ambient temperature, an insulated cabin was built in the laboratory, shown in figure 13. It was divided into two compartments; one is temperature controlled containing the vacuum chamber and some of the electronic equipment, the second compartment houses the rest of the measurement apparatus. The vacuum pump system was subsequently replaced due to a technical failure and placed outside the cabin.

Figure 13. A temperature stabilized cabin was built in the laboratory to solve the problems of temperature stability of the environment, and to allow for measurements at different temperatures. The vacuum chamber, not yet installed into the cabin, is seen to the right.

Although the dewars are expected to be good reflectors, their temperature is not controlled. Some modifications and improvements were therefore made to the experimental equipment and measurement routine. Notably, a polished copper container in good thermal contact with the vacuum chamber replaced the gold plated half spherical dewars. The emissivity coefficient of polished copper is around $\varepsilon = 0.1$ compared to gold where $\varepsilon = 0.02$ [22]. This seems to anchor the temperature of the radiative heat transfer reference, although loosing some efficiency in the reflectivity. A representative stability of the copper housing and the cabin temperature is demonstrated in figure 14. Stability conditions were introduced to activate a measurement, and the temperature of the laboratory, cabin and vacuum container were simultaneously measured.

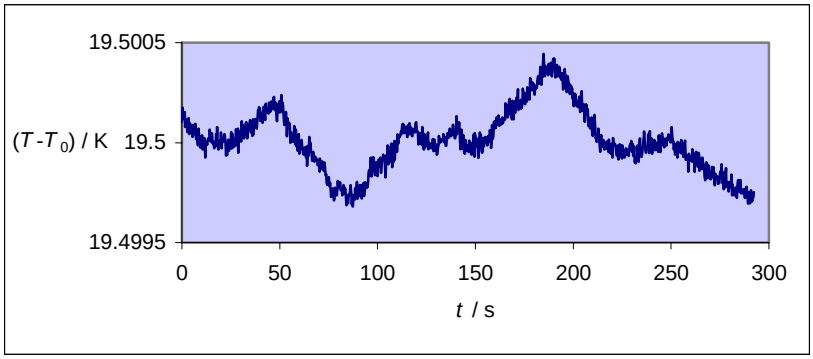

Figure 14-a. Temperature stability of the insulating cabin during a scan. The temperature variation is about 1 mK.

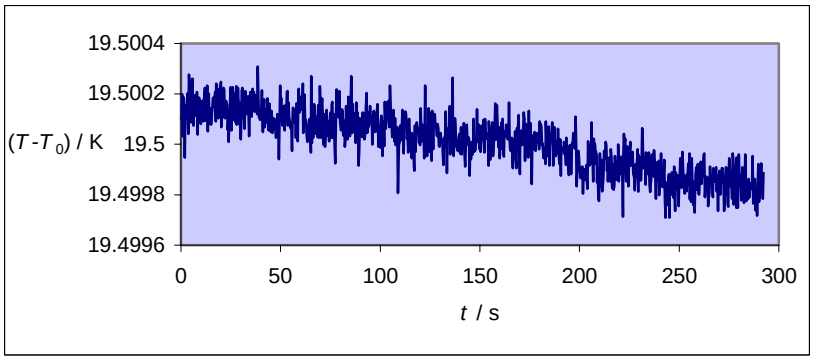

Figure 14-b. Temperature stability of the copper container during a scan. The temperature variation is about 400 µK.

The graphite sample and its housing are represented schematically in figure 15-a. The sample is placed on a wooden support and surrounded by a solid copper cylinder which is in thermal contact with the vacuum chamber, which in turn is thermally insulated. Two thermistors, *c.f.* figure 15-b, are connected via a resistance bridge device to a nV-meter, communicating via an interface (GPIB card) with a computer. The heating thermistor is piloted via an in-house interface connected to a high-speed digital acquisition card by the same computer.

Different acquisition times have been tested. The present measurements uses an acquisition speed of the bridge signal of typically 3.5 Hz; with one measurement lasting about five minutes. The DAQ card is piloted at an acquisition speed of 500 samples/s. Using a heating time of 60 s, the loss of an entire interval of the DAQ data will give rise to a relative uncertainty of 3 parts in 10^5.

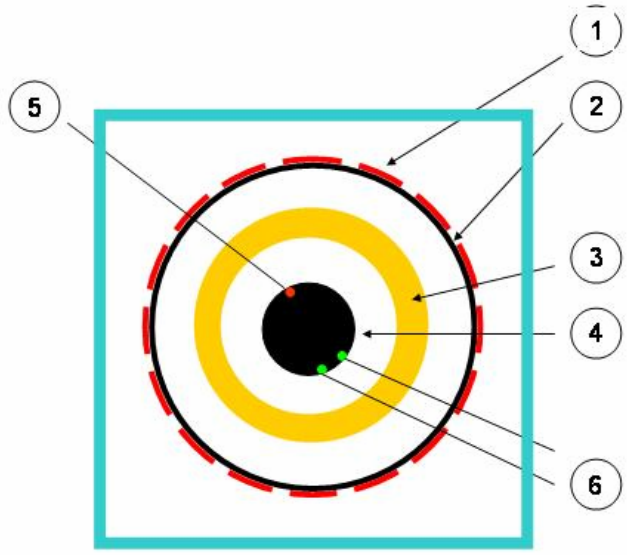

Figure 15-a. Top view of the graphite sample (4), equipped with one heating thermistor (5) and two sensor thermistors (6). Surrounded by a solid copper cylinder (3), the ensemble is placed inside a vacuum chamber (2), equipped with heating elements (1).

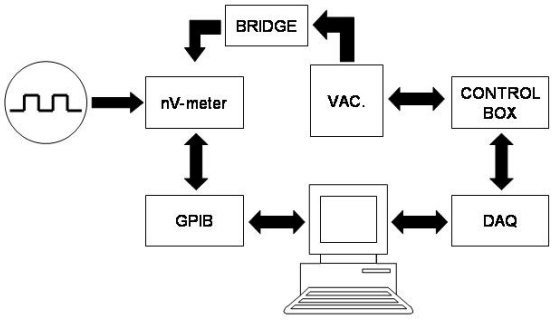

Figure 15-b. Flow chart of data collection. A computer, equipped with a GPIB card and a digital acquisition card controls the heating process. It also collects the data from the bridge via an externally triggered nV-meter and analyses the data to calculate the energy input.

3. Analysis method

3.1 Calculation of temperature rise using an empirical model

The main task is to determine the temperature rise ΔT of the graphite sample. If no losses are present, ΔT can be represented by the quantity indicated in figure 2-b; that is, the extrapolated temperature rise at $t_\Delta = t_{1/2} = (t_1+t_2)/2$, the extrapolated temperature difference at $t_\Delta = t_{1/2}$. This applies equally if the pre- and post-heating data have the same non-zero slope.

As mentioned earlier, losses will be present as soon as a temperature difference is introduced between the sample and the surrounding. The losses manifest themselves as a change in slope before and after heating, and for extreme losses a non-linearity may be evident. The problem is then to determine the value of ΔT if no losses were present. The analysis is complicated by the fact that heat transfer has a comparatively large time constant as shown in figure 10 and the position of the rising slope in time is offset from the heat input (t_1 and t_2). In other words, the extrapolated temperature rise at $t_{1/2}$ does not correspond to the true ΔT. Additionally, non-linear varying heat-loss due to external temperature gradients may introduce a systematic uncertainty. It is hence evident that a reduction of heat loss, as outlined in section 2.3.3., will decrease both statistical and systematic uncertainties.

The dynamics of a macroscopic temperature system can be modelled by the heat conduction equation, which have been applied by Domen and Lamperti [23] and Janssens et al. [24], with a set of first-order differential equations which in matrix form can be written as

$$\mathbf{C}\dot{\mathbf{T}} = \mathbf{P} - \mathbf{K}\mathbf{T}. \tag{10}$$

Here **C**, **P**, **K** and **T** represent the specific heat capacity, the power dissipated in the medium, the heat transfer coefficients and the temperature, respectively. A unique solution can be found for (10). However, two difficulties arise. Firstly, the laboratory temperature is far from stable. If the laboratory temperature has a non-linear drift, the laboratory temperature

variations will add a systematic uncertainty in the calculation of ΔT. Secondly, heat flow via radiation loss is present, which will add a parameter proportional to T^4. This can be written in matrix form as

$$\mathbf{C}\dot{\mathbf{T}} = \mathbf{P} - \mathbf{K}\mathbf{T} - \boldsymbol{\varepsilon}\mathbf{T}^4, \tag{11}$$

where $\boldsymbol{\varepsilon}$ represents a coefficient matrix combining emissivity and geometrical factors. The differential equation is no longer linear, nor homogenous. To obtain a unique solution, the resulting Riccati equation must be solved, which is not possible using elementary techniques [25].

Many numerical approaches have been made to calculate ΔT [26], of which some are based on extrapolation. Several methods were tested in these experiments, which led to the development of a physical empirical model: using four parameters that can be varied consisting of the initial graphite temperature, the ambient temperature, a cooling coefficient and a heat input coefficient, a temperature curve as a function of time is calculated representing the temperature behaviour in time close to the heating thermistor. A fifth parameter representing a combination of the heat diffusivity and an averaged geometry is added, which can be varied but, being a material constant, it should be considered fixed for a specific dimension. The graphite is divided into ten virtual elements, the heat being transported from element to element, representing the temperature along one dimension in the graphite sample from the heating thermistor to the sensing thermistors. The method makes use of the fact that the times at which heat is switched on and off are precisely known, *c.f.* figure 10. The variation of parameters continues until a satisfying agreement is achieved (in terms of pre- and post-heating) between the experimental curve and that representing the sensors. Using the final heat input coefficient, the unperturbed temperature rise ΔT can be calculated.

A measured temperature curve is shown in figure 16-a. The difference between post- and pre-heat loss is here about 300 µK/min, while the graphite has been heated by 12 mK approximately. A goodness of fit using the empirical model is demonstrated in figure 16-b, where the residuals T_{res}, representing the temperature difference between the measured and the calculated temperature curve, are plotted as a function of time.

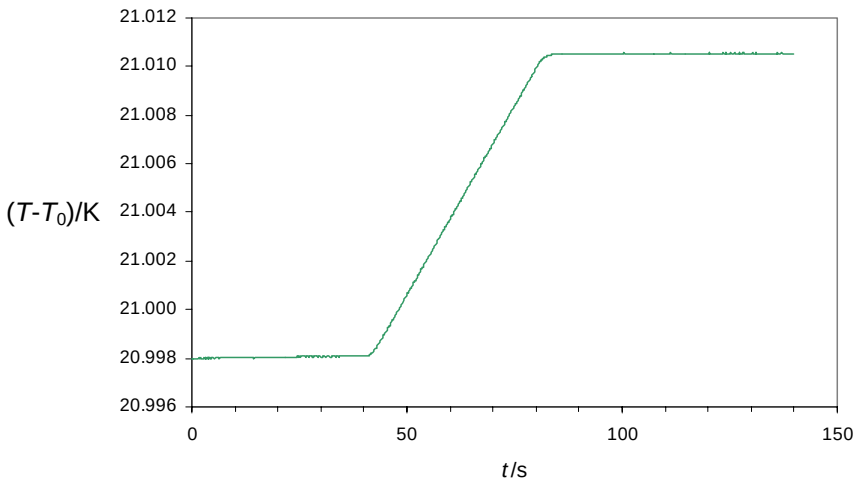

Figure 16-a.
Experimental temperature curve.

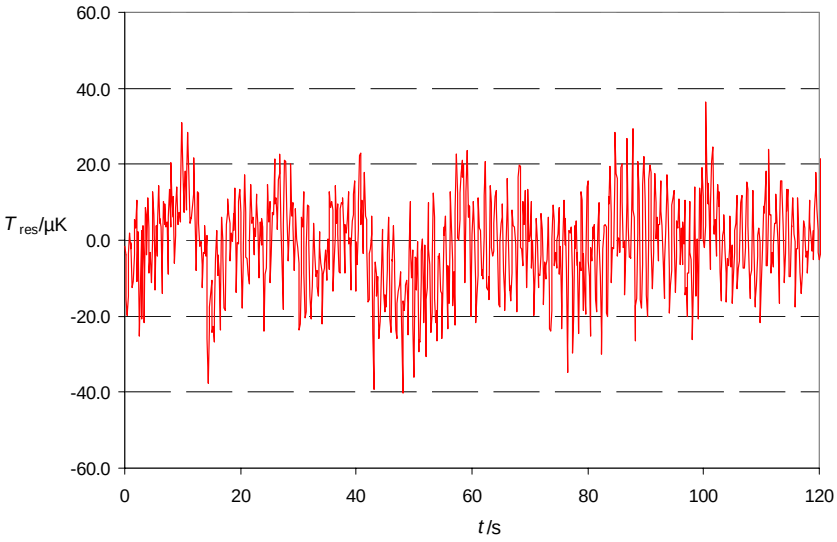

Figure 16-b. Temperature difference T_{res} between the measured (*c.f.* figure 16-a) and the calculated temperature curve using the empirical model as a function of time.

The root-mean-square uncertainty is here about 10 μK. An undulation can be observed during the first 40 s (pre-heating period), which may indicate a lack of temperature stability of the surrounding.

3.2 Impurity contributions

The relation between injected energy, E, and the specific heat capacity of graphite, $c_{p,g}$, can be written as

$$E = \Delta T \cdot m \cdot c_{p,g}, \tag{12}$$

where ΔT is the temperature increase of the graphite sample and m represents its mass. However, any material present not being graphite will also absorb a part of the injected energy. Regarding those materials as impurities, the relation (12) becomes

$$E = \Delta T \cdot m \cdot \left[c_{p,g} + \sum_i \frac{c_{p,i} \cdot m_i}{m} \right], \tag{13}$$

where the index i distinguishes each impurity. This means that the measured specific heat capacity must be corrected for impurities. To correct in an exact way, the mass and the specific heat capacity of each impurity must be known. In practice, the specific heat capacities are not well known and for that reason the mass of impurities must be reduced to the point where the uncertainty of the impurity correction becomes acceptable.

Table 3. Impurity contributions for graphite sample $\mathcal{H}$. The mass (m), absolute uncertainty (u) and specific heat capacity (c_p) are given for graphite (index g) and for the different impurities (index i).

material	i	m_g /g	$u(m_g)$/mg	$c_{p,g}$ /(J kg^{-1}K^{-1})		($c_{p,g} \times m_g$)/(J K^{-1})	
Graphite →		38.2553	0.5	700		26.8	
Impurity ↓		m_i /mg	$u(m_i)$/mg	$c_{p,i}$ /(J kg^{-1}K^{-1})	$u(c_{p,i})$/(J kg^{-1}K^{-1})	($c_{p,i} \times m_i$)/(J K^{-1})	$u(c_{p,i} \times m_i)$/(J K^{-1})
glass	} 1 bead	0.4	0.1	840	100	3.4×10^{-4}	9×10^{-5}
platinum (Pt)		0.1	0.1	130	10	1×10^{-5}	1×10^{-5}
1 bead		0.5	0.05	620	200	3.1×10^{-4}	6×10^{-5}
3 beads	**1**	**1.5**	**0.09**	**620**	**200**	$\mathbf{9.3 \times 10^{-4}}$	$\mathbf{3 \times 10^{-4}}$
adhesive	**2**	**7.5**	**0.05**	**1000**	**200**	$\mathbf{7.5 \times 10^{-3}}$	$\mathbf{1.5 \times 10^{-3}}$
wire wound	**3**	**54**	**2.0**	**950**	**200**	$\mathbf{51 \times 10^{-3}}$	$\mathbf{11 \times 10^{-3}}$
$\sum_i$						5.9×10^{-2}	1.1×10^{-2}

A thermistor bead placed inside the graphite core is connected by fine metal wires to the measurement equipment. It is necessary to consider the extent to which the wires should be included as impurities. In the present analysis it is assumed that only that section of the wire wound around the sample, which is in direct contact with graphite contributes to the impurity.

Assuming that the material heated is represented by the graphite cylinder $\mathcal{B}1$ and everything it contains, including the windings, table 3 shows the physical data of interest to establish an impurity correction and its uncertainty. The correction factor for $c_{p,g}$ of the measured graphite sample $\mathcal{H}$ is therefore

$$\left[\sum_k \frac{c_{i,k} \cdot m_{i,k}}{m}\right] = \frac{5.9\times10^{-2}}{38.25\times10^{-3}} = 1.54 \text{ J kg}^{-1}\text{K}^{-1}, \tag{14}$$

with an uncertainty u_i of

$$u_i = \frac{1.1\times10^{-2}}{38.25\times10^{-3}} = 0.29 \text{ J kg}^{-1}\text{K}^{-1}. \tag{15}$$

The uncertainty of the impurity correction will contribute about 4×10^{-4} to the relative systematic uncertainty.

4. Results

To test the method, the graphite sample $\mathcal{H}$ was measured. A small drift in c_p was observed when consecutive scans were made without waiting for the whole system to stabilize. The ΔT is calculated through linear extrapolation and assuming that the loss is proportional to ΔT - when the losses become important, neither the curves, nor the losses are linear any longer. Therefore, the whole system was allowed to stabilize at different temperatures according to pre-defined stability conditions. The sample was heated only when these conditions were fulfilled. Nearly 200 measurements were recorded, giving 20 averaged values of c_p at different constant temperatures from 19 °C to 25 °C. These data, where the uncertainty bars represent the standard uncertainty, are shown in the graph of figure 17. A linear curve was fitted to these data, where

$$c_p(\mathcal{H}, T) = 712.1(1) + 2.99(4)(T - 22.0 - 273.15) \quad \text{J kg}^{-1}\text{K}^{-1}. \tag{16}$$

The temperature T is given in K and the statistical uncertainty in the last digit of the linear parameters is indicated within parenthesis. The root-mean-square uncertainty of the fitted curve is 0.3 J $\text{kg}^{-1}\text{K}^{-1}$, corresponding to a relative standard uncertainty of the mean of 1 part in 10^4. An uncertainty budget was established, presented in table 4, where most of the contributions have been discussed in the previous sections. Applying the impurity correction factor (14) and the uncertainty budget, one obtains

$$c_{p,g}(\mathcal{H},T) = 710.6 + 3.0(T - 22 - 273.15) \quad \text{J kg}^{-1}\text{K}^{-1}, \tag{17}$$

with $u_c(c_{p,g}) = 0.7$ J kg^{-1}K^{-1}.

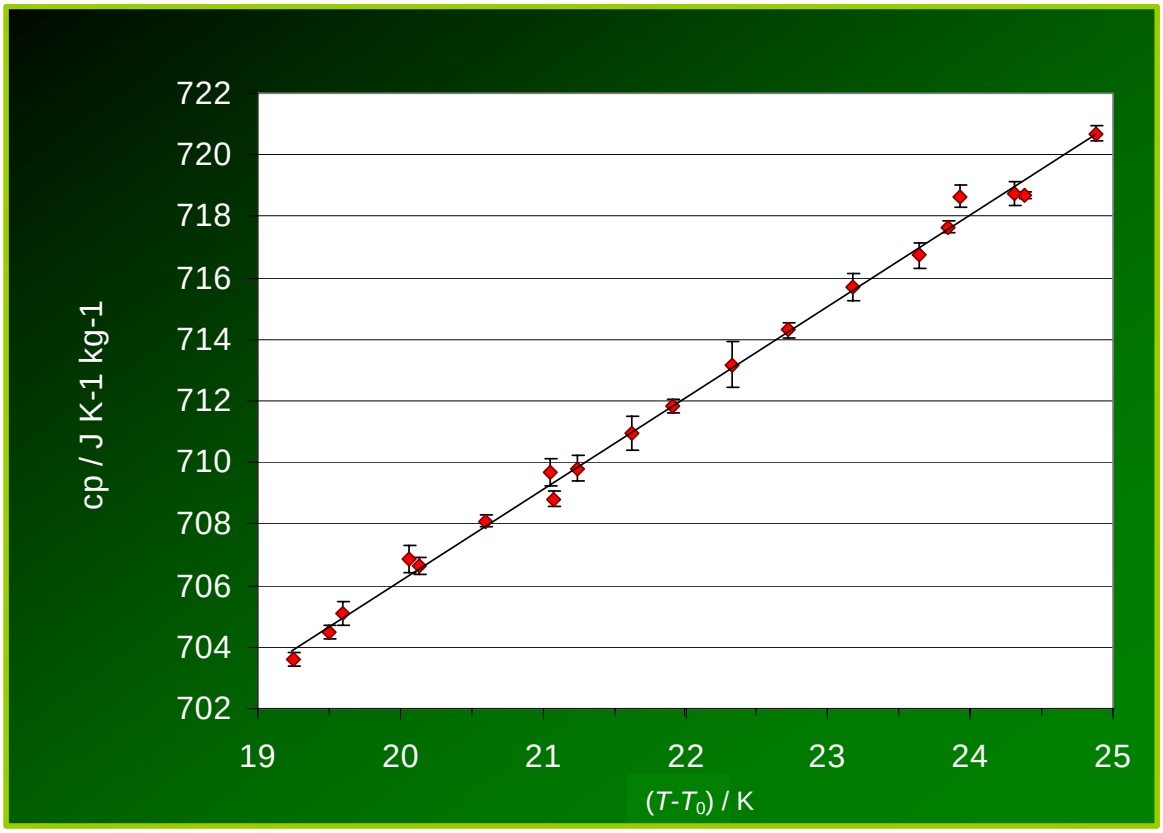

Figure 17. Measured heat capacity c_p for graphite as a function of temperature, obtained from sample $\mathcal{H}$.

Table 4. Uncertainty budget for the measurement of the specific heat capacity c_p of a single graphite sample, for a temperature range from 19 °C to 25 °C.

statistical uncertainties u_A	$u_A(y)/y$
integration method of power	3×10^{-5}
automated signal recognition of integration	6×10^{-8}
energy determination $(S/N)^{-1}$	1×10^{-5}
time stability	2×10^{-6}
mass	1×10^{-5}
bridge $(S/N)^{-1}$	1×10^{-4}
extrapolation for ΔT	5×10^{-4}
absolute ΔT	2×10^{-4}
total u_A	$\mathbf{5.5 \times 10^{-4}}$

systematic uncertainties u_B	$u_B(y)/y$
heating circuit resistance	1×10^{-4}
absolute T	3×10^{-5}
nV-meter calibration	3×10^{-5}
impurity correction	4×10^{-4}
one dimensional analysis method	3×10^{-4}
thermal drifts	6×10^{-4}
total u_B	$\mathbf{7.9 \times 10^{-4}}$

$u_c(y)/y$	$\mathbf{9.6 \times 10^{-4}}$

5. Discussion

Different values of the specific heat capacity of graphite at room temperature can be found in literature. In Table 5, some values for different types of graphite are listed where the constants correspond to

$$c_p(T) = \alpha + \beta \cdot (T - T_0) \quad \text{J kg}^{-1}\text{K}^{-1}, \qquad (18).$$

Table 5. Some published values of specific heat capacity of different types of graphite.

$c_p(T)$ / (J kg^{-1}K^{-1})	(T -273.15)/ K	β / (J kg^{-1}K^{-2})	type	
706	23.8	—	CS grade	[27]
639	22.6	—	Ceylon natural graphite	[28]
670-750	25.0	1.6-2.8	Graphite and pyrolytic carbon of a range of densities.	[29]
703	22.0	2.2		[30]
707.1	22.0	2.86		[31]
709.6	22.0	2.94		[12]
710.7	22.0	3.0		[this work]

The constant α is purely a reference for the curve and is not given in the table. The dispersion of the values of c_p and β is partly linked to different methods of measurement and analysis. They are also dependent on the purity and fabrication process of the graphite [32,33]. The most recent and precise determination of c_p and β known to us is reported by the NPL [12]. Comparing the values given in [12, 31] and obtained from this work, the spread is reasonable as the graphite manufacturers are different.

The uncertainty contribution for statistical uncertainties as presented in table 4 corresponds well with the root-mean-square uncertainty, 4 parts in 10^4 in relative terms.

The estimated systematic uncertainty is more difficult to predict. One part is definitely linked to parameters which must be calibrated. Effects induced by ambient temperature variations have been radically reduced. In spite of this, a small change of c_p as a function of the pre-heating drift was observed. A systematic contribution to the relative uncertainty of 6 parts in 10^4 was calculated, arising from the possible ambiguity of the system being in a steady or only quasi-static state, and that linear loss is assumed in the empirical model. An additional margin of a systematic contribution of 3 parts in 10^4 is introduced for the possible effect for the one-dimensional analysis.

Efforts to insulate the experimental equipment thermally have indeed reduced the overall uncertainties which were present at the start. The thermal stability obtained in the measurements now permits the determination of the increase of energy injected in the empirical model, as a consequence of the temperature dependence of the heating thermistor.

The largest obvious limiting factors are linked to systematic effects, notably in the interpretation of the temperature curves. A methodical study of the influence of the remaining drift may reduce this uncertainty. A better understanding of the temperature curves may be realized using finite element methods. Such an analysis would be a combination of the application of the heat equation and the empirical model. We intend to implement and test such a method in the near future.

6. Conclusion

The specific heat capacity of a graphite sample has been determined with a relative uncertainty better than 1 part in 10^3, where the largest limiting factors are linked to systematic effects. At this level, the measurement of the specific heat capacity for graphite is not the limiting factor in the determination of absorbed dose to water using a graphite calorimeter.

Acknowledgement

The authors are grateful to S. Duane and H. Palmans at the NPL and to A. Ostrovsky and J. Daures at the LNE-LNHB for helpful advice and discussion. Our appreciation goes to L. Erard, member of the CIPM, who initiated a contact with B. Hay and F. Haloua, LNE, with whom we also have had a stimulating exchange.

References

[1] Hemminger W and Höhne G, *Calorimety – Fundamentals and Practice* 1984 (Weinheim: Verlag Chemie)

[2] Höhne G, Hemminger W and Flammersheim H.-J. 1996 *Differential scanning calorimetry – an introduction for practitioners* (Berlin: Springer-Verlag)

[3] McEwen M R 2002 Development of a portable graphite calorimeter for measuring absorbed dose in the radiotherapy clinic (Univ. Surrey: Thesis)

[4] DuSautoy A R 2000 *Workshop on Recent Advances in Calorimetric Absorbed Dose Standards* ed A J Williams and K E Rosser (Teddington: National Physical Laboratory) pp 22-5

[5] Ross C K and Klassen N V 1996 Water calorimetry for radiation dosimetry *Phys. Med. Biol.* **41** 1-29

[6] Domen S R 1987 Advances in calorimetry for radiation dosimetry in *The dosimetry for ionizing radiation* Vol II Eds Kase K R, Bjärngard B E and Attix F H (New York: Academic Press) pp. 245-320

[7] 2001 Radiation dosimetry: X rays and gamma rays with maximum photon energies between 0.6 and 50 MeV *ICRU Report 64* (Bethesda MD: International Commission on Radiation Units and Measurements)

[8] 1977 Comité consultative pour les étalons de mesure des rayonnements ionisants, Section I *Report of 4th meeting of section I* (Sèvres: Bureau International de Poids et Mesures)

[9] 1988 Comité consultative pour les étalons de mesure des rayonnements ionisants, Section I *Report of 10th meeting of section I* (Sèvres: Bureau International de Poids et Mesures)

[10] 1969 Radiation dosimetry: X rays and gamma rays with maximum photon energies between 0.6 and 50 MeV *ICRU Report 14* (Washington D.C.: International Commission on Radiation Units and Measurements)

[11] Saifun Huq M and Andreo P 2004 Advances in the determination of absorbed dose to water in clinical high-energy photon and electron beams using ionization chambers, and references therein *Phys. Med. Biol.* **49** R49-R104

[12] Williams A J, Burns D T and McEwen M R1993 Measurement of the specific heat capacity of the electron-beam graphite calorimeter *NPL Report RSA(EXT) 40* (Teddington: National Physical Laboratory)

[13] Gupta S V 2002 Practical density measurement and hydrometry (Bristol: Institute of Physics Publishing)

[14] 2001 Standard test method for bulk density of as-manufactured carbon and

graphite shapes C838-96 (West Conshohocken: ASTM International)

[15] 2000 Standard practice for heat flow calibration of differential scanning calorimeters C559-90 (West Conshohocken: ASTM International)

[16] Giacomo P 1982 Equation for the determination of the density of moist air (1981) *Metrologia* **18** 33-40

[17] Davis R S 1992 Equation for the determination of the density of moist air (1981/91) *Metrologia* **29** 67-70

[18] 1995 Guide to the expression of uncertainty in measurement (Geneva: International Organisation for Standardization)

[19] Sanders R P and Thomas C G 1991 A precision voltage supply for the NPL primary-standard electron-beam calorimeter. *NPL Report RSA(EXT) 24* (Teddington: National Physical Laboratory)

[20] Allan D W 1966 Statistics and atomic frequency standard *IEEE Procedings* **54** 221-31

[21] 1989 Handbook of applied thermal design ed Guyer E C (New York: McGraw-Hill Book Company)

[22] Siegel R and Howell J R 1981 Thermal radiation heat transfer (Washington: McGraw-Hill Book Company)

[23] Domen S R and Lamperti P J 1974 A heat-loss-compensated calorimeter: Theory, design and performance *J. Res. Nat. Bur. Stand.* **78A** 595-610

[24] Janssens A, Cottens E, Paulsen A and Poffijn A 1986 Equilibrium of a graphite absorbed-dose colorimeter and the quasi-isothermal mode of operation *Metrologia* **22** 265-70

[25] Harris J W and Stocker H 1998 Handbook of mathematics and computational science (New York: Springer-Verlag)

[26] Gunn S R 1971 On the calculation of the corrected temperature rise in isoperibol calorimetry. Modifications of the Dickinson extrapolation method and treatment of thermistor-thermistor resistance values *J. Chem. Thermodynamics* **3** 19-34

[27] DeSorbo W and Tyler W W 1953 The specific heat of graphite from 13° to 300°K *J. Chem. Phys.* **21** 1660-3

[28] DeSorbo W 1955 Low temperature heat capacity of Ceylon graphite *J. Am. Chem. Soc.* **75** 4713-5

[29] Lutcov A I, Volga V I and Dymov B K 1970 Thermal conductyivity, electric resistivity and specific heat of dense graphites *Carbon* **8** 733-60

[30] Dinsdale A T 1991 SGTE data for pure elements *Calphad* **15** 317-425

[31] Burns D T and Morris W T 1991 A graphite calorimeter for electron beam dosimetry *High dose dosimetry for radiation processing Proc. IAEA* **IAEA-SM-314/33** 123-36

[32] Kelly B T 1981 Physics of graphite (London: Applied Science Publishers)

[33] Mantell C L 1968 Carbon and graphite handbook (New York: John Wiley & sons)